
Sparse Data Generation Using Diffusion Models

Phil Ostheimer
RPTU Kaiserslautern-Landau
ostheimer@cs.uni-kl.de

Mayank Nagda
RPTU Kaiserslautern-Landau
nagda@cs.uni-kl.de

Jean Radig
Heidelberg University
jean.radig@uni-heidelberg.de

Carl Herrmann
Heidelberg University
carl.herrmann@uni-heidelberg.de

Stephan Mandt
University of California, Irvine
mandt@uci.edu

Marius Kloft
RPTU Kaiserslautern-Landau
kloft@cs.uni-kl.de

Sophie Fellenz
RPTU Kaiserslautern-Landau
fellenz@cs.uni-kl.de

Abstract

Sparse data is ubiquitous, appearing in numerous domains, from economics and recommender systems to astronomy and biomedical sciences. However, efficiently generating high-fidelity synthetic sparse data remains a significant challenge. We introduce Sparse Data Diffusion (SDD), a novel method for generating sparse data. SDD extends continuous state-space diffusion models with an explicit representation of exact zeros by modeling sparsity through the introduction of Sparsity Bits. Empirical validation in various domains—including two scientific applications in physics and biology—demonstrates that SDD achieves high fidelity in representing data sparsity while preserving the quality of the generated data.

1 Introduction

Sparse data—i.e., data where most values are zero—is a fundamental challenge in many real-world applications. Sparsity arises naturally—for instance, in neural recordings where only a few neurons spike at any moment, or in recommender systems where users engage with only a handful of items. In physics, calorimeter images from high-energy experiments record energy deposits in only a few localized regions, corresponding to particle interactions. In biology, single-cell RNA (scRNA) data exhibit sparsity because each cell expresses only a subset of genes [23, 24, 18].

The importance of sparsity has long been recognized. As Donoho [4] famously noted in his work on compressed sensing, most data “can be thrown away”, highlighting that a small number of active components governs many real-world phenomena. Tibshirani [41] further emphasized this insight in the context of linear modeling with the Lasso, arguing that sparsity is not merely a theoretical convenience but a practical assumption—reflecting the reality that, in many problems, only a small subset of variables is truly relevant.

Generative models have revolutionized artificial intelligence by enabling systems to create realistic, high-dimensional data across many applications. Techniques such as Generative Adversarial Networks (GANs) [6], Variational Autoencoders (VAEs) [17], and more recently Diffusion Models (DMs)

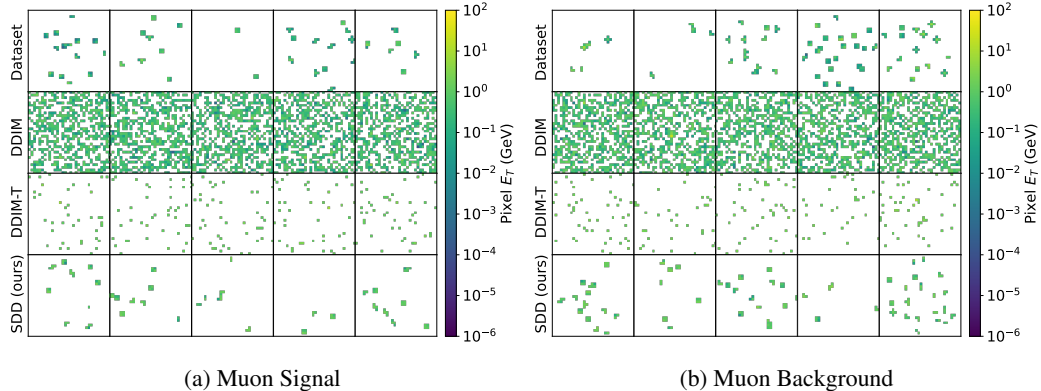


Figure 1: Calorimeter images for the muon isolation study: signal (left) vs. background (right). From top to bottom: (1) real data, (2) DDIM, (3) DDIM thresholded to match the dataset’s sparsity (DDIM-T), and (4) SDD (ours). Pixel intensity (GeV) shows energy deposits, with white = zero. DDIM and DDIM-T miss the sparse, localized patterns, whereas SDD closely reproduces the true physical structure.

[37, 14, 38, 1] have pushed the boundaries of what machines can generate, achieving state-of-the-art performance in domains such as image and audio synthesis.

Despite their success in dense domains, diffusion models fundamentally mismatch inherently sparse data—adding Gaussian noise to every dimension assumes smooth, recoverable perturbations, but true zeros encode meaningful absence (e.g., a silent gene or non-firing neuron) and become indistinguishable from weak signal once noised. Their isotropic noise processes, smooth denoising networks, and activations (ReLU [28], Tanh, Sigmoid [20]) bias outputs toward density, leading DDIM to produce only 49% sparsity on data that is 95% sparse (Fig. 1), with thresholding (DDIM-T) to match the dataset’s sparsity still failing to recover clustered structures. In contrast, classical methods like Lasso [41] explicitly model zeros, underscoring the need for generative models that treat sparsity as a first-class objective rather than a post-hoc correction, especially in scientific domains where sparse patterns carry crucial information.

To bridge this gap, we introduce Sparse Data Diffusion (SDD), a generative framework that explicitly models sparsity. At its core, SDD uses *Sparsity Bits* (SBs)—discrete latent variables that indicate, for each output dimension, whether it should be active or zero. The dense values are modeled using a continuous state-space diffusion process, preserving the versatility and performance benefits of continuous over discrete diffusion models. During sampling, SBs are applied to enforce sparsity. Additionally, SBs make the output more interpretable, as they can be easily visualized and interpreted separately from the dense output. We evaluate the proposed approach in challenging data domains from physics, biology, and computer vision. In summary, we make the following contributions:

- We introduce SDD, a novel generative framework that enforces output sparsity in diffusion models through a dedicated sparsity representation.
- We propose Sparsity Bits—latent variables that model sparsity explicitly—and integrate them with a continuous state-space diffusion process for dense values, enabling joint modeling of structure and content; moreover, we provide theoretical guarantees demonstrating the efficacy of Sparsity Bits in preserving true-zero patterns.
- We validate SDD on sparse datasets from physics, biology, and computer vision, achieving substantial improvements over standard diffusion models.

2 Related work

As no broadly applicable generative model for sparse data exists, our section on related work summarizes existing domain-specific works on sparse data generation, related concepts in diffusion models, and enforcing sparsity in neural model parameters (and not the data itself).

Sparse data generation Past work on sparse, *continuous* data generation focuses on simple architectures and specific applications, such as calorimeter sensor data in physics, which are incomparable to recent state-of-the-art generative models. They decouple the sparsity information for generating data by introducing decoupled generative models where the sparsity is introduced as a learnable Dirac delta mass at zero [23, 24]. Other works focusing on sparse, *discrete* data generation use Poisson or negative binomial distributions to model sparse count data with bursts [45, 35]. There are also deep variants [5, 9, 36]. However, as already indicated, they are not applicable to our setting, which has continuous sparse data that do not exhibit the traits of a Poisson or negative binomial distribution.

Diffusion models Diffusion models can be broadly categorized into continuous state-space models [37, 14, 38, 39] for continuous data and discrete state-space models [1, 8] for discrete data. While discrete state-space diffusion models can model sparse discrete data exactly, they are not applicable to our setting, which involves sparse continuous data. Some continuous state-space diffusion models, such as Bit Diffusion [2], have demonstrated strong performance on discrete data, even surpassing discrete models. Others, like Unigs [30] and DefectSpectrum [44], handle both continuous and discrete data by first encoding discrete variables into continuous representations before diffusion. However, these approaches do not diffuse continuous and discrete variables jointly. In contrast, our method uniquely enables simultaneous diffusion of both variable types in a unified framework.

Enforcing sparsity Sparsity is not just an inherent trait in datasets that can be, e.g., exploited to store data efficiently. Sparsity can also help in the model architecture. Previous work [12, 42] shows that neural networks are greatly overparameterized and multiple methods [27, 22, 40, 21] *inter alia* have been introduced to mitigate this overparameterization by sparsifying the underlying neural network weights. Others [15] leverage this property to efficiently train low-rank decomposition matrices, which are added as sparse weight updates to the existing model weights. However, these methods focus on enforcing sparsity in the model weights and are therefore not applicable to our setting, where we enforce sparsity in the model output.

3 Method

This section presents Sparse Data Diffusion (SDD), a novel framework designed for the generation of sparse data. We begin by introducing the underlying statistical model, followed by an in-depth explanation of the forward and backward diffusion processes, and the overall training and sampling procedure. We conclude this section with a theoretical analysis on why SDD actually works.

3.1 Statistical model

The following statistical model forms the basis for SDD: Let $\mathbf{x}_0 \sim p$ with $\mathbb{E}[\mathbf{x}_0] < \infty$ and $\mathbf{x}_0 \in \mathbb{R}^d$, where p is unknown and arbitrary. We infer the sparsity for each dimension by applying the indicator function element-wise to \mathbf{x}_0 :

$$\bar{\mathbf{x}}_0 = 2 * \mathbb{1}_{x \neq 0}(\mathbf{x}_0) - 1 \quad (1)$$

As a result, $\bar{\mathbf{x}}_0 \in \{-1, 1\}^d$ is a binary vector that encodes, for each element in \mathbf{x}_0 , whether it is zero or represents a dense value. Therefore, we refer to each element in $\bar{\mathbf{x}}_0$ as a *Sparsity Bit (SB)*. We obtain the extended input $\hat{\mathbf{x}}_0 \in \mathbb{R}^{2d}$, where $\hat{\mathbf{x}}_0 \sim \hat{p}$, by concatenating $\mathbf{x}_0 \in \mathbb{R}^d$ and $\bar{\mathbf{x}}$:

$$\hat{\mathbf{x}}_0 = \langle \mathbf{x}_0, \bar{\mathbf{x}}_0 \rangle \quad (2)$$

Unlike prior methods, our forward-backward process diffuses continuous and discrete variables jointly. Previous work operated either only on continuous variables [37, 14, 38, 39] or on discrete variables [2].

Forward diffusion The forward diffusion process follows previous work [37, 14, 38, 39]. It consists of a predefined series of transitions from the input space $\hat{\mathbf{x}}_0 \in \mathbb{R}^{2d}$ to pure noise $\epsilon \in \mathbb{R}^{2d}$, where $\epsilon \sim \mathcal{N}(0, I)$. The transition from $\hat{\mathbf{x}}_0$ to $\hat{\mathbf{x}}_t$ is defined as

$$\hat{\mathbf{x}}_t = \sqrt{\alpha(t)}\hat{\mathbf{x}}_0 + \sqrt{1 - \alpha(t)}\epsilon, \quad (3)$$

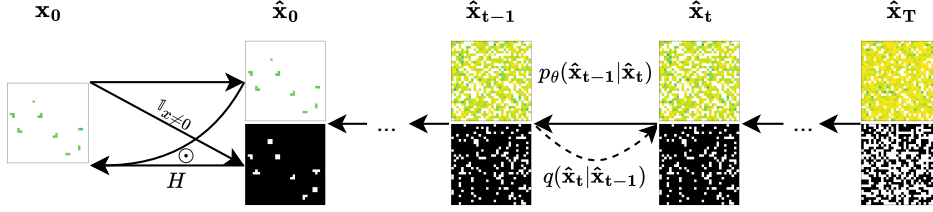


Figure 2: Shown is an illustration of our method SDD. Compared to other diffusion models, we expand the continuous input by discrete Sparsity Bits for forward diffusion and use them in backward diffusion and sampling to enforce sparsity in the data.

where $\epsilon \sim \mathcal{N}(0, I)$, $t \sim \mathcal{U}(0, T)$ is a continuous time variable, and α is the noise schedule, a monotonically decreasing function from 1 to 0. In the limit, we obtain:

$$\lim_{T \rightarrow \infty} \hat{\mathbf{x}}_T = \epsilon \sim \mathcal{N}(0, I), \quad (4)$$

Backward diffusion The backward diffusion process consists of steps that reverse the forward diffusion process: $\hat{\mathbf{x}}_T \rightarrow \hat{\mathbf{x}}_{T-\Delta} \rightarrow \dots \rightarrow \hat{\mathbf{x}}_0$. These steps follow a normal distribution:

$$\hat{\mathbf{x}}_{t-1} | \hat{\mathbf{x}}_t \sim \mathcal{N}(\mu_t(\hat{\mathbf{x}}_t, \hat{\mathbf{x}}_0), \sigma_t^2) \quad (5)$$

where $\hat{\mathbf{x}}_0$ is the denoised input. Since $\hat{\mathbf{x}}_0$ is not given in the backward diffusion process, we train a denoising neural network f_θ to predict $\hat{\mathbf{x}}_0$. We describe the training process in the following Section 3.2 and illustrate our model in Figure 2.

3.2 Training

In order to perform the steps $\hat{\mathbf{x}}_T \rightarrow \hat{\mathbf{x}}_{T-\Delta} \rightarrow \dots \rightarrow \hat{\mathbf{x}}_0$ of the backward diffusion process, we train a denoising network f_θ to predict $\hat{\mathbf{x}}_0$, which is part of the distribution $p(\hat{\mathbf{x}}_{t-1} | \hat{\mathbf{x}}_t)$. The predicted value of $\hat{\mathbf{x}}_0$ is approximated by $\tilde{\mathbf{x}}_0 = f_\theta(\hat{\mathbf{x}}_t, t)$ (alternative formulations predict the noise ϵ).

We use self-conditioning [2] to incorporate the previously computed $\tilde{\mathbf{x}}_0$ (or $\tilde{\epsilon}$) from time step $t + 1$ to compute the next $\tilde{\mathbf{x}}_0$ (or $\tilde{\epsilon}$). The training is realized using an l_2 regression loss on the continuous inputs and a cross entropy loss (CE on labels in $\{-1, 1\}$) on SBs:

$$\mathcal{L}(\theta) = \mathbb{E} \left[\|f_{\theta, 0:d-1}(\hat{\mathbf{x}}_t, t, \tilde{\mathbf{x}}_0) - \hat{\mathbf{x}}_{0, 0:d-1}\|^2 + \text{CE}(f_{\theta, d:2d-1}(\hat{\mathbf{x}}_t, t, \tilde{\mathbf{x}}_0), \hat{\mathbf{x}}_{0, d:2d-1}) \right], \quad (6)$$

where $\hat{\mathbf{x}}_0 \sim \hat{p}$, $t \sim \mathcal{U}(0, T)$, $\epsilon \sim \mathcal{N}(0, I)$ and $\mathbf{x}_t = \sqrt{\alpha(t)}\hat{\mathbf{x}}_0 + \sqrt{1 - \alpha(t)}\epsilon$. We summarize the SDD training process in Algorithm 1 in Appendix A.

3.3 Sampling

To draw samples, we use the same state transitions as described in the backward diffusion process: $\hat{\mathbf{x}}_T \rightarrow \hat{\mathbf{x}}_{T-\Delta} \rightarrow \dots \rightarrow \hat{\mathbf{x}}_0$, following $p(\hat{\mathbf{x}}_{t-1} | \hat{\mathbf{x}}_t)$ using $f_\theta(\hat{\mathbf{x}}_t, t, \tilde{\mathbf{x}}_0)$. There are multiple ways to perform these steps. Here, we focus on Denoising Diffusion Probabilistic Models (DDPM) [14] and Denoising Diffusion Implicit Models (DDIM) [38].

We perform one final step: $\hat{\mathbf{x}}_0 \rightarrow \mathbf{x}_0$. Since the first d dimensions in $\hat{\mathbf{x}}_0$ contain the dense and second d dimensions in $\hat{\mathbf{x}}_0$ contain the SBs, we quantize the SB output dimensions $\hat{\mathbf{x}}_{0, d:(2d-1)}$ using the heaviside step function H applied element-wise to extract the SBs. Afterward, we apply an element-wise product to get the sparsified output:

$$\mathbf{x}_0 = \hat{\mathbf{x}}_{0, 0:(d-1)} \odot H(\hat{\mathbf{x}}_{0, d:(2d-1)}) \quad (7)$$

We summarize the sampling algorithm in Algorithm 2 in Appendix A.

3.4 Why do sparsity bits work?

We show that SBs give an error-controlled atom at zero. Let $\bar{x}_{0,i} \in \{0, 1\}$ be the ground-truth SB for coordinate i (0 denotes an exact zero). Define the model’s predicted bit by $\hat{x}_{0,i} = H(s_i)$, where $s_i = f_{\theta,d+i}(\hat{\mathbf{x}}_t, t)$ is the SB logit and H is the Heaviside step. Write

$$\rho_i := \Pr[\bar{x}_{0,i} = 0], \quad \hat{\rho}_i := \Pr[\hat{x}_{0,i} = 0], \quad \varepsilon_i := \Pr[\bar{x}_{0,i} \neq \hat{x}_{0,i}].$$

Proposition 1 (Total-variation control). *For each dimension i we have the exact inequality*

$$|\hat{\rho}_i - \rho_i| \leq \varepsilon_i.$$

Consequently, if the SB classification error ε_i tends to 0 during training, the probability that the model outputs an exact zero converges to the true sparsity ρ_i .

Proof. Partition the sample space into the four disjoint events generated by the pair $(\bar{x}_{0,i}, \hat{x}_{0,i})$:

$$E_{00}, E_{01}, E_{10}, E_{11} \quad \text{with} \quad E_{ab} = \{\bar{x}_{0,i} = a, \hat{x}_{0,i} = b\}.$$

Then $\rho_i = \Pr[E_{00}] + \Pr[E_{01}]$, $\hat{\rho}_i = \Pr[E_{00}] + \Pr[E_{10}]$, and the mis-classification probability is $\varepsilon_i = \Pr[E_{01}] + \Pr[E_{10}]$. Hence

$$|\hat{\rho}_i - \rho_i| = |\Pr[E_{10}] - \Pr[E_{01}]| \leq \Pr[E_{10}] + \Pr[E_{01}] = \varepsilon_i. \quad \square$$

Interpretation and practical considerations The bound is tight and assumption-free: any reduction in the SB error ε_i *directly* tightens the gap between the model’s exact-zero probability $\hat{\rho}_i$ and the true sparsity ρ_i . In practice, we use the l_2 loss in Equation (6) across the whole state-space for simplicity and compatibility with other continuous state-space diffusion models.

4 Experiments

To evaluate SDD for sparse data generation, we begin by analyzing the general sparsity characteristics of the generated data. We then present results from challenging real-world applications in the sciences, with a focus on physics and biology. Finally, we provide a deeper analysis of sparse image generation.

4.1 Experimental setup

Baselines We compare SDD to two state-of-the-art diffusion models—DDPM [14] and DDIM [38]. While these models are originally designed to generate dense data, our focus is on their performance in producing sparse outputs. We adapt them to our setting and introduce thresholded variants, DDPM-T and DDIM-T, which apply a post hoc procedure to match the average sparsity of the training data. Specifically, we iteratively increase a threshold—linearly spaced between zero and the maximum output value—and zero out all values below it until the sparsity of the generated samples approximately matches the training data. This thresholding procedure serves as a pragmatic baseline for adapting diffusion models to sparse domains. Applying a threshold zeroes out small values, forcing the output to match the dataset’s sparsity level. While this post hoc method lacks explicit modeling of sparsity during training, it offers a meaningful baseline for evaluating the advantages of sparsity-aware models like SDD.

Datasets In the domain of physics, we focus on sparse data arising from particle physics experiments. Specifically, we use calorimeter images from a muon isolation study [23], which exhibit high sparsity (approximately 95%) and are represented as 32×32 pixel grids. The intensity of each pixel represents the energy deposited in a specific cell, which is the sum of momenta transverse to the beam (P_T) of particles that hit that calorimeter cell. The dataset consists of 33,331 signal images of isolated muons and 30,783 background images of muons produced in association with a jet. We experiment with two single-cell RNA (scRNA) datasets: the Tabula Muris dataset [34] with 57K cells (with 90% sparsity, 98% when filtered to the 1000 most highly variable genes) and the Human Lung Pulmonary Fibrosis dataset [10] with 114K cells (with 91% sparsity, 96% when filtered to the 1000 most highly variable genes). For sparse image generation, we use MNIST [19] (with 81% sparsity) and Fashion-MNIST [43] (with 50% sparsity), both containing 60,000 gray-scale training images of size 28×28 each. We apply standard pre-processing to all datasets by linearly scaling input values to the range $[-1, 1]$ following Ho et al. [14]. After model inference, we apply an inverse transformation.

Evaluation We evaluate how the sparsity distribution matches the real data. In addition, we use domain-specific evaluation metrics: In the physics domain, we evaluate the generated calorimeter images by computing the Wasserstein Distance W_P between the distributions of sum of momenta transverse to the beam P_T and invariant mass for the entire dataset and 50,000 generated calorimeter images, as in previous work [23, 24]. For scRNA data, we use, in line with previous work [25], the following metrics: Spearman Correlation Coefficient (SCC), Pearson Correlation Coefficient (PCC), the Maximum Mean Discrepancy (MMD) [7], and the Local Inverse Simpson’s index (LISI) [11] comparing the real dataset to 10,000 generated cells. For sparse image generation, we analyze the sparsity of pixels (after discretization by thresholding logit values in $[-1, 1]$ to discrete values in $[0, 255]$) and compare them to the sparsity within the dataset. The primary evaluation metric for images is the Fréchet Inception Distance (FID) [13] calculated between 50,000 generated images and the entire training set. However, the standard Inception network used to compute FID was trained only on dense images from ImageNet [3], limiting its validity for sparse data. We report FID only for completeness.

Architecture We use the Convolutional Neural Network (CNN) based U-Net architecture as in previous work [14, 33, 29]. We apply this architecture to all considered models for calorimeter image and sparse image generation, as the underlying data have a similar size. We use a base channel dimension of 256, three stages, and two residual blocks per stage, with a total of 37M parameters. For sparse data generation of scRNA data, we follow scDiffusion [25] and use a Multi-Layer Perceptron (MLP) with skip connections with a total of 5M parameters, as scRNA data lacks the spatial structure of images. We further analyze the number of additional parameters and the runtime overhead in Appendix B.

Other settings We use Adam [16] for optimization. We train 300K steps per task for image and scRNA generation and 200K steps for calorimeter image generation with a constant learning rate of 0.0002 and a batch size of 256. An exponential moving average of the parameters is used to improve training dynamics with a decay factor of 0.9999. We use a fixed number of 1000 steps for sampling and DDIM and DDPM.

4.2 Evaluating the recovery of ground truth sparsity patterns

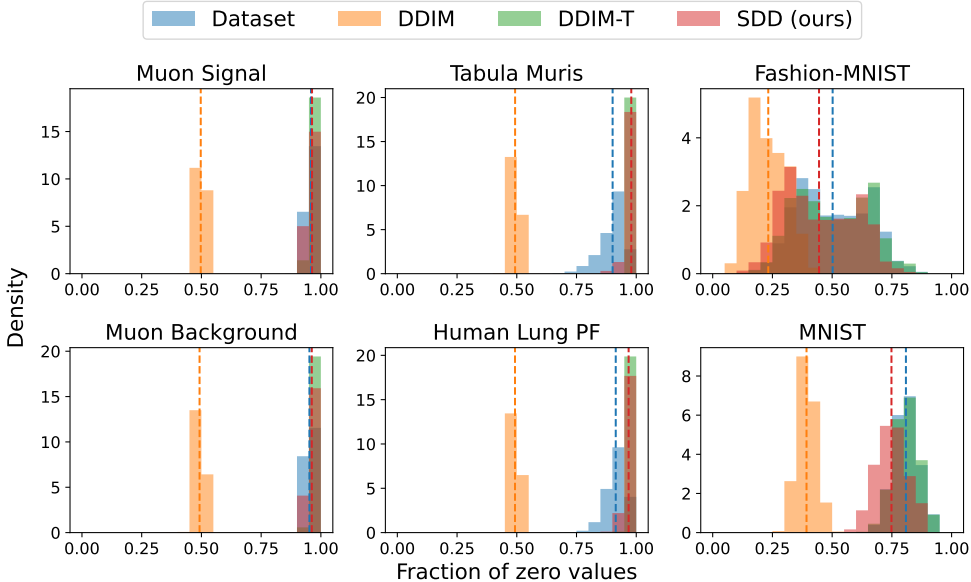


Figure 3: Sparsity distribution of real and generated data. Shown are sparsity histograms (20 bins) and average sparsity levels (dashed vertical lines) for the real dataset and samples generated by DDIM, DDIM-T, and the proposed SDD. DDIM significantly underestimates sparsity, while DDIM-T overshoots in the upper range and lacks distributional diversity. In contrast, SDD more closely matches the real data’s sparsity profile.

How well do models match ground-truth sparsity? We analyze the sparsity distribution of generated samples in Figure 3 for DDIM. The results for DDPM can be found in Appendix C, mostly matching those of DDIM. Across all datasets, DDIM consistently underestimates sparsity. In contrast, DDIM-T overshoots the upper end of the sparsity distribution while truncating the lower end, particularly for the two sparse image generation datasets. SDD more closely matches the real data’s distribution: it slightly overshoots sparsity in the physics datasets (Muon Signal and Muon Background) and, to a greater extent, in the scRNA datasets (Tabula Muris and Human Lung Pulmonary Fibrosis), though still less than DDIM-T. For the vision datasets (Fashion-MNIST and MNIST), SDD reproduces a broader and more faithful sparsity distribution.

In general, diffusion models struggle to generate sparse data. If the standard post-processing step—clipping values to the range $[-1, 1]$ followed by rescaling—is omitted, the resulting samples exhibit near-zero sparsity across all datasets. As this clipping step is standard practice in diffusion-based models, we retain it and focus our subsequent analyses on clipped outputs.

Consequences of sparsity mismatch in scientific and vision tasks Identifying the particle source of a particular detector signature is one of the most important tasks in particle physics [23, 24]. As shown, DDIM and DDIM-T fail to reproduce the sparsity patterns of the data. This discrepancy is especially evident in Figure 1, where both models produce significantly denser outputs, leading to an inflated number of apparent particle detections and thus, incorrect physical interpretations.

In scRNA, sparsity arises from biologically meaningful dropout events. DDIM-generated samples capture only about half the true sparsity levels, misrepresenting dropout structure and undermining downstream analyses that rely on it—such as sparsity-aware clustering or gene expression imputation [31]. Although DDIM-T achieves the correct average sparsity, it fails in quantitative evaluations (see Section 4.4), suggesting that superficial matching of sparsity levels is insufficient

In sparse image generation, the impact of sparsity mismatch may appear less critical at first glance. However, applications like fake image detection rely on subtle cues such as sparsity structure. When generated images lack these traits, detection becomes trivial—compromising model robustness and undermining security-sensitive applications.

Sharpness of generated SBs As SBs are central to SDD and our model is the first one to simultaneously diffuse the discrete SBs and continuous (dense) inputs, we further examine the distribution of the logits for the SBs in Figure 7 in Appendix C. As can be seen, SBs are sharply distributed towards -1 and 1, indicating the model’s confidence in predicting these pixel values as zero or non-zero. This indicates that discrete variables can be reliably diffused alongside continuous variables. The last bin with an upper bound of 1.0 shows almost precisely the pixel sparsity of the respective dataset.

4.3 Physics: calorimeter image generation

Quantitative evaluation The results are summarized in Table 1. The Wasserstein Distance W_p between the distributions of the sum of momenta transverse to the beam P_T for both signal and background images is much greater for DDPM and DDIM as well as for the thresholded DDPM-T and DDIM-T, but with a smaller gap, compared to SDD DDPM and SDD DDIM, indicating that the latter models generate distributions that more closely match the real data. Similarly, the W_p for the invariant mass is larger for DDPM and DDIM, and still larger for DDPM-T and DDIM-T across both signal and background images when compared to SDD DDPM and SDD DDIM, further demonstrating the improved fidelity of SDD. These results suggest that SDD is better aligned with the true data distribution, ultimately improving the quality and realism of the generated calorimeter images.

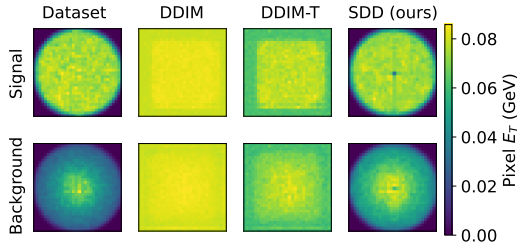


Figure 4: Shown are the average calorimeter images for Muon Signal and Muon Background. DDIM and DDIM-T fail to generate realistic data, while SDD succeeds. Linear scale to reveal the signal and background differences.

Table 1: Shown are the results for sparse calorimeter image generation. SDD performs better in preserving the key structural properties of the data: sum of momenta transverse to the beam P_T and invariant mass.

MODEL	SIGNAL		BACKGROUND	
	$\downarrow P_T$	$\downarrow \text{MASS}$	$\downarrow P_T$	$\downarrow \text{MASS}$
DDPM	199.52	67.19	187.58	64.80
DDIM	221.35	74.78	270.24	92.64
DDPM-T	38.01	12.71	32.68	12.95
DDIM-T	41.95	14.42	36.98	14.24
SDD DDPM	20.68	5.66	9.05	3.29
SDD DDIM	20.81	5.60	14.12	3.91

Table 2: The results for sparse data generation on scRNA data are shown. SDD outperforms DDPM and DDIM and the thresholded DDPM-T and DDIM-T in all considered metrics.

MODEL	$\uparrow \text{SCC}$	TABULA MURIS			$\uparrow \text{LISI}$	$\uparrow \text{SCC}$	HUMAN LUNG PF		
		$\uparrow \text{PCC}$	$\downarrow \text{MMD}$	$\downarrow \text{MMD}$			$\uparrow \text{PCC}$	$\downarrow \text{MMD}$	$\uparrow \text{LISI}$
DDPM	0.49	0.72	3.58	0.00	0.31	0.85	3.35	0.00	
DDIM	0.50	0.74	3.62	0.00	0.30	0.87	3.34	0.00	
DDPM-T	0.53	0.68	0.25	0.01	0.31	0.82	0.69	0.00	
DDIM-T	0.56	0.73	0.24	0.01	0.28	0.85	0.65	0.00	
SDD DDPM	0.96	0.95	0.12	0.21	0.95	0.99	0.18	0.08	
SDD DDIM	0.97	0.97	0.12	0.23	0.95	0.99	0.18	0.08	

Qualitative evaluation We show example calorimeter images of isolated muons (signal) and muons produced in association with a jet (background) in Figure 1 for DDIM. Further results for DDPM can be found in Appendix D, mostly resembling those of DDIM. Figure 1 shows that DDIM-sampled images fail to reflect the pixel clusters with energy deposits, while the thresholded DDIM-T images have a lot more isolated energy deposits of single pixels. SDD reflects the pixel clusters of deposited energy in the generated calorimeter images. We also show the pixel-wise averages of the calorimeter images in Figure 4, underlining the superior performance of SDD compared to DDIM and DDIM-T, as DDIM and DDIM-T show a consistent level of detections in the whole average image. Also, SDD reflects the almost uniform distribution within the cylindrical shape of the calorimeter for signal images, while the background images show the muons produced from a jet that deposits energy close to the muon.

4.4 Biology: scRNA data generation

Quantitative evaluation For scRNA data generation, we summarize our results in Table 2. As seen on both datasets, Tabula Muris and Human Lung Pulmonary Fibrosis, SDD with DDPM and DDIM performs several magnitudes better than DDPM and DDIM as well as the thresholded DDPM-T and DDIM-T. SCC and PCC indicate that SDD has a more similar ordering and a “more linear” relationship between the average expression values of each gene compared to the dataset. The distance between the gene expression distributions measured by MMD indicates that the distance for SDD is much lower than for DDPM and DDIM as well as DDPM-T and DDIM-T. The mixing between real and generated data is indicated through the LISI score and shows that SDD produces expression values closer to the original dataset.

Qualitative evaluation In our qualitative evaluation for scRNA data we provide UMAPs [26] for Tabula Muris and Human Lung Pulmonary Fibrosis in Figure 5 for DDIM with a further analysis with similar results for DDPM in Appendix E. Both subfigures in Figure 5 show almost no overlap between real data and DDIM-generated data. For DDIM-T, the cluster of generated cells gets closer

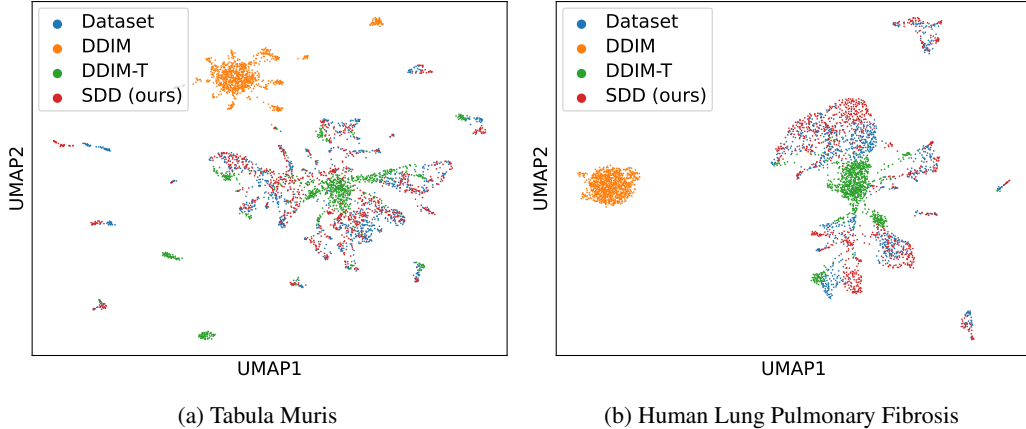


Figure 5: Shown are two-dimensional UMAPs of Tabula Muris and Human Lung Pulmonary Fibrosis, and the respective DDIM, DDIM-T, and SDD generated samples. DDIM and DDIM-T show little to no overlap with the respective dataset while SDD shows significant overlap, demonstrating that SDD more accurately captures the underlying structure and diversity of the real data distributions.

to real cells but shows little diversity. For SDD, we can see a significant overlap between real cells and those sampled from SDD, further underlining the high quality of generated cells.

4.5 Vision: sparse image generation

Quantitative evaluation For sparse image generation, we summarize our results in Table 4 in Appendix F. We observe similar FID scores for all settings considered. However, the validity of FID for evaluating sparse images is questionable, as the standard Inception network used to compute FID was trained only on dense images from ImageNet [3], which may limit its effectiveness for sparse data. Therefore, we report these values only for completeness.

Qualitative evaluation The quality of generated images on Fashion-MNIST and MNIST (see Figures 11 and 12 in Appendix F) is largely indistinguishable across DDIM, DDPM, their thresholded variants (DDIM-T, DDPM-T), and SDD using DDPM and DDIM. Visually, all models produce plausible samples. However, a closer inspection of the sparsity patterns reveals meaningful differences. In particular, SDD more faithfully reproduces the sparsity structure of the real data. For Fashion-MNIST, thresholded models like DDIM-T and DDPM-T tend to suppress fine-grained noisy regions near the edges. Similarly, in MNIST, the digits generated by DDIM-T and DDPM-T are generally narrower than those in real data. These subtle differences highlight that, while thresholding may yield visually appealing outputs, it often fails to preserve key structural properties of the data, particularly in challenging regions where sparsity transitions are critical. SDD, by contrast, maintains these characteristics more reliably, capturing both visual fidelity and underlying data distribution properties by explicitly modeling the sparsity.

5 Conclusion

We introduce SDD, a novel method for generating sparse data using diffusion models. The core idea is to represent sparsity on a per-dimension basis using Sparsity Bits—discrete variables—and to diffuse these alongside the continuous input variables within a shared continuous state space, thereby preserving the model’s versatility. We provide theoretical guarantees demonstrating that Sparsity Bits reliably recover true-zero patterns, and we empirically show that this approach is both interpretable and flexible across tasks in physics, biology, and vision. SDD achieves high fidelity in representing data sparsity while maintaining the quality of generated samples, outperforming traditional diffusion models that tend to produce unrealistic reconstructions when applied to sparse data. However, despite enforcing sparsity in the generated data, our current implementation does not exploit this property for computational efficiency, e.g., it does not reduce storage or accelerate inference by skipping

zeros. Another limitation is the strong assumption that sparsity corresponds strictly to exact zeros; in practice, “sparse” may refer to values merely close to zero.

Our work enables explicit encoding of sparsity in state-of-the-art generative models, making it particularly valuable for domains where real data is inherently sparse, such as physics and biology. The underlying concept of SBs can also be integrated into other generative models, including GANs [6], VAEs [17], and Normalizing Flows [32], thereby opening up new research directions. As with any generative modeling approach, there is also a potential risk of misuse, such as generating misleading or synthetic data that could be misinterpreted in scientific analyses. Further exploration could focus on refining the techniques used to enforce sparsity within these models, enhancing their efficiency and applicability across various scientific fields.

References

- [1] Jacob Austin, Daniel D. Johnson, Jonathan Ho, Daniel Tarlow, and Rianne van den Berg. Structured denoising diffusion models in discrete state-spaces. In Marc’Aurelio Ranzato, Alina Beygelzimer, Yann N. Dauphin, Percy Liang, and Jennifer Wortman Vaughan, editors, *Advances in Neural Information Processing Systems 34: Annual Conference on Neural Information Processing Systems 2021, NeurIPS 2021, December 6-14, 2021, virtual*, pages 17981–17993, 2021. URL <https://proceedings.neurips.cc/paper/2021/hash/958c530554f78bcd8e97125b70e6973d-Abstract.html>.
- [2] Ting Chen, Ruixiang Zhang, and Geoffrey E. Hinton. Analog bits: Generating discrete data using diffusion models with self-conditioning. In *The Eleventh International Conference on Learning Representations, ICLR 2023, Kigali, Rwanda, May 1-5, 2023*. OpenReview.net, 2023. URL <https://openreview.net/forum?id=3itjR9QxFw>.
- [3] Jia Deng, Wei Dong, Richard Socher, Li-Jia Li, Kai Li, and Li Fei-Fei. Imagenet: A large-scale hierarchical image database. In *2009 IEEE conference on computer vision and pattern recognition*, pages 248–255. Ieee, 2009.
- [4] David L. Donoho. Compressed sensing. *IEEE Trans. Inf. Theory*, 52(4):1289–1306, 2006. doi: 10.1109/TIT.2006.871582. URL <https://doi.org/10.1109/TIT.2006.871582>.
- [5] Chengyue Gong et al. Deep dynamic Poisson factorization model. *Advances in Neural Information Processing Systems*, 30, 2017.
- [6] Ian Goodfellow, Jean Pouget-Abadie, Mehdi Mirza, Bing Xu, David Warde-Farley, Sherjil Ozair, Aaron Courville, and Yoshua Bengio. Generative adversarial networks. *Communications of the ACM*, 63(11):139–144, 2020.
- [7] Arthur Gretton, Karsten M Borgwardt, Malte J Rasch, Bernhard Schölkopf, and Alexander Smola. A kernel two-sample test. *The Journal of Machine Learning Research*, 13(1):723–773, 2012.
- [8] Shuyang Gu, Dong Chen, Jianmin Bao, Fang Wen, Bo Zhang, Dongdong Chen, Lu Yuan, and Baining Guo. Vector quantized diffusion model for text-to-image synthesis. In *IEEE/CVF Conference on Computer Vision and Pattern Recognition, CVPR 2022, New Orleans, LA, USA, June 18-24, 2022*, pages 10686–10696. IEEE, 2022. doi: 10.1109/CVPR52688.2022.01043. URL <https://doi.org/10.1109/CVPR52688.2022.01043>.
- [9] Dandan Guo, Bo Chen, Hao Zhang, and Mingyuan Zhou. Deep poisson gamma dynamical systems. *Advances in Neural Information Processing Systems*, 31, 2018.
- [10] Arun C Habermann, Austin J Gutierrez, Linh T Bui, Stephanie L Yahn, Nichelle I Winters, Carla L Calvi, Lance Peter, Mei-I Chung, Chase J Taylor, Christopher Jetter, et al. Single-cell rna sequencing reveals profibrotic roles of distinct epithelial and mesenchymal lineages in pulmonary fibrosis. *Science advances*, 6(28):eaba1972, 2020.
- [11] Laleh Haghverdi, Aaron TL Lun, Michael D Morgan, and John C Marioni. Batch effects in single-cell rna-sequencing data are corrected by matching mutual nearest neighbors. *Nature biotechnology*, 36(5):421–427, 2018.

- [12] Song Han, Huizi Mao, and William J. Dally. Deep compression: Compressing deep neural network with pruning, trained quantization and Huffman coding. *arXiv: Computer Vision and Pattern Recognition*, 2015. URL <https://api.semanticscholar.org/CorpusID:2134321>.
- [13] Martin Heusel, Hubert Ramsauer, Thomas Unterthiner, Bernhard Nessler, and Sepp Hochreiter. GANs trained by a two time-scale update rule converge to a local Nash equilibrium. In Isabelle Guyon, Ulrike von Luxburg, Samy Bengio, Hanna M. Wallach, Rob Fergus, S. V. N. Vishwanathan, and Roman Garnett, editors, *Advances in Neural Information Processing Systems 30: Annual Conference on Neural Information Processing Systems 2017, December 4-9, 2017, Long Beach, CA, USA*, pages 6626–6637, 2017. URL <https://proceedings.neurips.cc/paper/2017/hash/8a1d694707eb0fefe65871369074926d-Abstract.html>.
- [14] Jonathan Ho, Ajay Jain, and Pieter Abbeel. Denoising diffusion probabilistic models. In Hugo Larochelle, Marc’Aurelio Ranzato, Raia Hadsell, Maria-Florina Balcan, and Hsuan-Tien Lin, editors, *Advances in Neural Information Processing Systems 33: Annual Conference on Neural Information Processing Systems 2020, NeurIPS 2020, December 6-12, 2020, virtual*, 2020. URL <https://proceedings.neurips.cc/paper/2020/hash/4c5bcfec8584af0d967f1ab10179ca4b-Abstract.html>.
- [15] Edward J Hu, yelong shen, Phillip Wallis, Zeyuan Allen-Zhu, Yuanzhi Li, Shean Wang, Lu Wang, and Weizhu Chen. LoRA: low-rank adaptation of large language models. In *International Conference on Learning Representations*, 2022. URL <https://openreview.net/forum?id=nZeVKeeFYf9>.
- [16] Diederik P. Kingma and Jimmy Ba. Adam: A method for stochastic optimization. In Yoshua Bengio and Yann LeCun, editors, *3rd International Conference on Learning Representations, ICLR 2015, San Diego, CA, USA, May 7-9, 2015, Conference Track Proceedings*, 2015. URL <http://arxiv.org/abs/1412.6980>.
- [17] Diederik P Kingma and Max Welling. Auto-encoding variational Bayes, 2014. URL <https://arxiv.org/abs/1312.6114>.
- [18] David Lähnemann, Johannes Köster, Ewa Szczurek, Davis J McCarthy, Stephanie C Hicks, Mark D Robinson, Catalina A Vallejos, Kieran R Campbell, Niko Beerenwinkel, Ahmed Mahfouz, et al. Eleven grand challenges in single-cell data science. *Genome biology*, 21:1–35, 2020.
- [19] Yann LeCun. The mnist database of handwritten digits. <http://yann.lecun.com/exdb/mnist/>, 1998.
- [20] Yann LeCun, Léon Bottou, Genevieve B. Orr, and Klaus-Robert Müller. Efficient backprop. In Grégoire Montavon, Genevieve B. Orr, and Klaus-Robert Müller, editors, *Neural Networks: Tricks of the Trade - Second Edition*, volume 7700 of *Lecture Notes in Computer Science*, pages 9–48. Springer, 2012. doi: 10.1007/978-3-642-35289-8_3. URL https://doi.org/10.1007/978-3-642-35289-8_3.
- [21] Namhoon Lee, Thalaiyasingam Ajanthan, and Philip H. S. Torr. SNIP: Single-shot network pruning based on connection sensitivity. *ArXiv*, abs/1810.02340, 2018. URL <https://api.semanticscholar.org/CorpusID:52920837>.
- [22] Christos Louizos, Max Welling, and Diederik P. Kingma. Learning sparse neural networks through l0 regularization. In *International Conference on Learning Representations*, 2018. URL <https://openreview.net/forum?id=H1Y8hhg0b>.
- [23] Yadong Lu, Julian Collado, Kevin Bauer, Daniel Whiteson, and Pierre Baldi. Sparse image generation with decoupled generative models. In *Neural Information Processing Systems, Machine Learning and the Physical Sciences Workshop*, 2019.
- [24] Yadong Lu, Julian Collado, Daniel Whiteson, and Pierre Baldi. Sparse autoregressive models for scalable generation of sparse images in particle physics. *Physical Review D*, 103(3):036012, 2021.

- [25] Erpai Luo, Minsheng Hao, Lei Wei, and Xuegong Zhang. scdiffusion: conditional generation of high-quality single-cell data using diffusion model. *Bioinformatics*, 40(9):btac518, 2024.
- [26] Leland McInnes and John Healy. UMAP: uniform manifold approximation and projection for dimension reduction. *CoRR*, abs/1802.03426, 2018. URL <http://arxiv.org/abs/1802.03426>.
- [27] Dmitry Molchanov, Arsenii Ashukha, and Dmitry Vetrov. Variational dropout sparsifies deep neural networks. In Doina Precup and Yee Whye Teh, editors, *Proceedings of the 34th International Conference on Machine Learning*, volume 70 of *Proceedings of Machine Learning Research*, pages 2498–2507. PMLR, 06–11 Aug 2017. URL <https://proceedings.mlr.press/v70/molchanov17a.html>.
- [28] Vinod Nair and Geoffrey E. Hinton. Rectified linear units improve restricted boltzmann machines. In Johannes Fürnkranz and Thorsten Joachims, editors, *Proceedings of the 27th International Conference on Machine Learning (ICML-10), June 21-24, 2010, Haifa, Israel*, pages 807–814. Omnipress, 2010. URL <https://icml.cc/Conferences/2010/papers/432.pdf>.
- [29] Alexander Quinn Nichol, Prafulla Dhariwal, Aditya Ramesh, Pranav Shyam, Pamela Mishkin, Bob McGrew, Ilya Sutskever, and Mark Chen. GLIDE: towards photorealistic image generation and editing with text-guided diffusion models. In Kamalika Chaudhuri, Stefanie Jegelka, Le Song, Csaba Szepesvári, Gang Niu, and Sivan Sabato, editors, *International Conference on Machine Learning, ICML 2022, 17-23 July 2022, Baltimore, Maryland, USA*, volume 162 of *Proceedings of Machine Learning Research*, pages 16784–16804. PMLR, 2022. URL <https://proceedings.mlr.press/v162/nichol22a.html>.
- [30] Lu Qi, Lehan Yang, Weidong Guo, Yu Xu, Bo Du, Varun Jampani, and Ming-Hsuan Yang. Unigs: Unified representation for image generation and segmentation. In *IEEE/CVF Conference on Computer Vision and Pattern Recognition, CVPR 2024, Seattle, WA, USA, June 16-22, 2024*, pages 6305–6315. IEEE, 2024. doi: 10.1109/CVPR52733.2024.00603. URL <https://doi.org/10.1109/CVPR52733.2024.00603>.
- [31] Peng Qiu. Embracing the dropouts in single-cell rna-seq analysis. *Nature communications*, 11(1):1169, 2020.
- [32] Danilo Jimenez Rezende and Shakir Mohamed. Variational inference with normalizing flows. In Francis R. Bach and David M. Blei, editors, *Proceedings of the 32nd International Conference on Machine Learning, ICML 2015, Lille, France, 6-11 July 2015*, volume 37 of *JMLR Workshop and Conference Proceedings*, pages 1530–1538. JMLR.org, 2015. URL <http://proceedings.mlr.press/v37/rezende15.html>.
- [33] Olaf Ronneberger, Philipp Fischer, and Thomas Brox. U-net: convolutional networks for biomedical image segmentation. In Nassir Navab, Joachim Hornegger, William M. Wells III, and Alejandro F. Frangi, editors, *Medical Image Computing and Computer-Assisted Intervention - MICCAI 2015 - 18th International Conference Munich, Germany, October 5 - 9, 2015, Proceedings, Part III*, volume 9351 of *Lecture Notes in Computer Science*, pages 234–241. Springer, 2015. doi: 10.1007/978-3-319-24574-4_28. URL https://doi.org/10.1007/978-3-319-24574-4_28.
- [34] Nicholas Schaum, Jim Karkanias, Norma F Neff, Andrew P May, Stephen R Quake, Tony Wyss-Coray, Spyros Darmanis, Joshua Batson, Olga Botvinnik, Michelle B Chen, et al. Single-cell transcriptomics of 20 mouse organs creates a tabula muris: The tabula muris consortium. *Nature*, 562(7727):367, 2018.
- [35] Aaron Schein, Hanna Wallach, and Mingyuan Zhou. Poisson-gamma dynamical systems. *Advances in Neural Information Processing Systems*, 29, 2016.
- [36] Aaron Schein, Scott W. Linderman, Mingyuan Zhou, David M. Blei, and Hanna M. Wallach. Poisson-randomized gamma dynamical systems. In Hanna M. Wallach, Hugo Larochelle, Alina Beygelzimer, Florence d’Alché-Buc, Emily B. Fox, and Roman Garnett, editors, *Advances in Neural Information Processing Systems 32: Annual Conference on Neural Information*

- Processing Systems 2019, NeurIPS 2019, December 8-14, 2019, Vancouver, BC, Canada*, pages 781–792, 2019. URL <https://proceedings.neurips.cc/paper/2019/hash/1543843a4723ed2ab08e18053ae6dc5b-Abstract.html>.
- [37] Jascha Sohl-Dickstein, Eric A. Weiss, Niru Maheswaranathan, and Surya Ganguli. Deep unsupervised learning using nonequilibrium thermodynamics. In Francis R. Bach and David M. Blei, editors, *Proceedings of the 32nd International Conference on Machine Learning, ICML 2015, Lille, France, 6-11 July 2015*, volume 37 of *JMLR Workshop and Conference Proceedings*, pages 2256–2265. JMLR.org, 2015. URL <http://proceedings.mlr.press/v37/sohl-dickstein15.html>.
- [38] Yang Song and Stefano Ermon. Improved techniques for training score-based generative models. In Hugo Larochelle, Marc’Aurelio Ranzato, Raia Hadsell, Maria-Florina Balcan, and Hsuan-Tien Lin, editors, *Advances in Neural Information Processing Systems 33: Annual Conference on Neural Information Processing Systems 2020, NeurIPS 2020, December 6-12, 2020, virtual*, 2020. URL <https://proceedings.neurips.cc/paper/2020/hash/92c3b916311a5517d9290576e3ea37ad-Abstract.html>.
- [39] Yang Song, Jascha Sohl-Dickstein, Diederik P. Kingma, Abhishek Kumar, Stefano Ermon, and Ben Poole. Score-based generative modeling through stochastic differential equations. In *9th International Conference on Learning Representations, ICLR 2021, Virtual Event, Austria, May 3-7, 2021*. OpenReview.net, 2021. URL <https://openreview.net/forum?id=PXTIG12RRHS>.
- [40] Mingjie Sun, Zhuang Liu, Anna Bair, and J. Zico Kolter. A simple and effective pruning approach for large language models. In *The Twelfth International Conference on Learning Representations, ICLR 2024, Vienna, Austria, May 7-11, 2024*. OpenReview.net, 2024. URL <https://openreview.net/forum?id=PxoFut3dWW>.
- [41] Robert Tibshirani. Regression shrinkage and selection via the lasso. *Journal of the Royal Statistical Society Series B: Statistical Methodology*, 58(1):267–288, 1996.
- [42] Karen Ullrich, Edward Meeds, and Max Welling. Soft weight-sharing for neural network compression. In *5th International Conference on Learning Representations, ICLR 2017, Toulon, France, April 24-26, 2017, Conference Track Proceedings*. OpenReview.net, 2017. URL <https://openreview.net/forum?id=HJGwcKc1x>.
- [43] Han Xiao, Kashif Rasul, and Roland Vollgraf. Fashion-mnist: a novel image dataset for benchmarking machine learning algorithms, 2017.
- [44] Shuai Yang, Zhifei Chen, Pengguang Chen, Xi Fang, Yixun Liang, Shu Liu, and Yingcong Chen. Defect spectrum: A granular look of large-scale defect datasets with rich semantics. In Ales Leonardis, Elisa Ricci, Stefan Roth, Olga Russakovsky, Torsten Sattler, and Gül Varol, editors, *Computer Vision - ECCV 2024 - 18th European Conference, Milan, Italy, September 29-October 4, 2024, Proceedings, Part VII*, volume 15065 of *Lecture Notes in Computer Science*, pages 187–203. Springer, 2024. doi: 10.1007/978-3-031-72667-5_11. URL https://doi.org/10.1007/978-3-031-72667-5_11.
- [45] Mingyuan Zhou and Lawrence Carin. Augment-and-conquer negative binomial processes. In Peter L. Bartlett, Fernando C. N. Pereira, Christopher J. C. Burges, Léon Bottou, and Kilian Q. Weinberger, editors, *Advances in Neural Information Processing Systems 25: 26th Annual Conference on Neural Information Processing Systems 2012. Proceedings of a meeting held December 3-6, 2012, Lake Tahoe, Nevada, United States*, pages 2555–2563, 2012. URL <https://proceedings.neurips.cc/paper/2012/hash/6a61d423d02a1c56250dc23ae7ff12f3-Abstract.html>.

A Training and sampling algorithms

In this section, we present SDD’s training procedure in Algorithm 1 and the sampling in Algorithm 2.

Algorithm 1 SDD training algorithm.

```
def train_loss(x):
    # Create & concat sparsity bits
    x_sb = (x != 0).float()
    x_sb = (x_sb * 2 - 1)
    x = (x * 2 - 1)
    x = cat((x, x_sb), dim=1)

    # Forward diffusion steps
    t = uniform(0, 1)
    eps = normal(mean=0, std=1)
    x_t = sqrt(alpha(t)) * x + (1 - sqrt(alpha(t))) * eps

    # Compute self-cond estimate.
    x_0 = zeros_like(x_t)
    if uniform(0, 1) > 0.5:
        x_0 = net(cat([x_t, x_0], -1), t)
        x_0 = stop_gradient(x_0)

    # Predict and compute loss.
    x_0 = net(cat([x_t, x_0], -1), t)
    l2_loss = (x_0[:, :sb] - x[:, :sb]) ** 2
    ce_loss = cross_entropy_loss(x_0[:, sb:] - x[:, sb:])
    return l2_loss.mean() + ce_loss.mean()
```

Algorithm 2 SDD sampling algorithm.

```
def sample(steps, interm=False):
    x_t = randn(mean=0, std=1)
    x_pred = zeros_like(x_t)

    for step in range(steps):
        # Get time for current & next states.
        t_now = 1 - step / steps
        t_next = max(1 - (step + 1)/steps, 0)

        # Predict x_0.
        x_pred = net(cat([x_t, x_pred], -1), t_now)

        # Estimate x at t_next.
        x_t = ddim_or_ddpm_step(x_t, x_pred, t_now, t_next)

    # Return sparsified data point
    x_pred.clamp_(-1,1)
    x_dense = (x_pred[:, :sb] + 1) / 2
    x_sb = (x_pred[:, sb:] > 0).float()
    x_sparse = x_dense * x_sb
    return x_sparse
```

B Compute resources and runtime analysis

SDD enforces sparsity in the generated data and does not exploit the data sparsity to make the computations more efficient. Depending on the underlying U-Net architecture, we have more trainable parameters. We use CNNs with a total of 37M parameters for the calorimeter and the sparse images. However, for SDD, we observe an increase of only 0.07% in the number of parameters. For sparse data generation of scRNA data with an MLP with a total of 5M parameters, we observe an increase of 38.37% in the number of parameters. The increase in the number of parameters is much higher, as we have to double the size of the input and output layers. At the same time, we only need to double the number of input and output channels for the CNN-based U-Net for images.

We summarize the training runtime of DDPM and SDD in Table 3. We omit DDIM as the DDPM and DDIM variants have the same training procedure. Our experiments were executed on a NVIDIA DGX-A100 server with eight A100 (40GB) GPUs and an AMD Epyc 7742 CPU with 64 cores. We measured runtimes per training step on one A100 (40GB) that show minimal overhead for SDD compared to DDPM, as additional computations are efficiently parallelized.

Table 3: Shown are the runtimes of DDPM compared to SDD. The overhead for SDD is minimal.

UNET	DATASET	DDPM	SDD
CNN	MNIST	0.57 s	0.56 s
CNN	FASHION-MNIST	0.50 s	0.51 s
CNN	MUON SIGNAL	0.56 s	0.56 s
CNN	MUON BACKGROUND	0.59 s	0.58 s
MLP	TABULA MURIS	0.02 s	0.02 s
MLP	HUMAN LUNG PULMONARY FIBROSIS	0.02 s	0.02 s

C Further evaluating the recovery of ground truth sparsity patterns

How well do models match ground-truth sparsity? We present the sparsity distribution of samples generated by DDPM in Figure 6, complementing the main text’s analysis of DDIM (Figure 3). The trends observed largely mirror those of DDIM. Specifically, DDPM also tends to underestimate sparsity across all datasets. Similar to DDIM-T, DDPM-T produces samples with an exaggerated upper tail in the sparsity distribution and a compressed lower end, particularly noticeable in the sparse image generation datasets. SDD remains the most faithful to the real data’s sparsity profile: it mildly overshoots in the physics datasets (Muon Signal and Muon Background) and does so more substantially in the scRNA datasets (Tabula Muris and Human Lung Pulmonary Fibrosis), though still less severely than DDPM-T. On the vision datasets (Fashion-MNIST and MNIST), SDD continues to generate a wider and more accurate sparsity distribution.

Sharpness of generated SBs Figure 7 illustrates the distribution of the sparsity bit (SB) logits across datasets. The histograms show that the logits are sharply concentrated near -1 and 1, indicating high model confidence when classifying each dimension as corresponding to a zero or non-zero pixel. This supports the feasibility of jointly diffusing discrete and continuous components. Moreover, the final bin (with upper bound 1.0) closely aligns with the true sparsity levels of each dataset: 95.2% for Muon Signal, 97.9% for Tabula Muris, 50.2% for Fashion-MNIST, 95.2% for Muon Background, 95.9% for Human Lung Pulmonary Fibrosis, and 80.9% for MNIST.

D Further results for physics: calorimeter image generation

Figure 8 presents example calorimeter images generated by DDPM for isolated muons (signal) and muons produced in association with jets (background). The observations are largely consistent with those reported for DDIM in Figure 1. Specifically, DDPM-generated images struggle to capture the characteristic clustered energy deposits, while the thresholded variant, DDPM-T, produces more isolated single-pixel activations. In contrast, SDD-DDPM generates images that more accurately reflect the spatial structure of energy clusters. Complementary pixel-wise average images, shown in

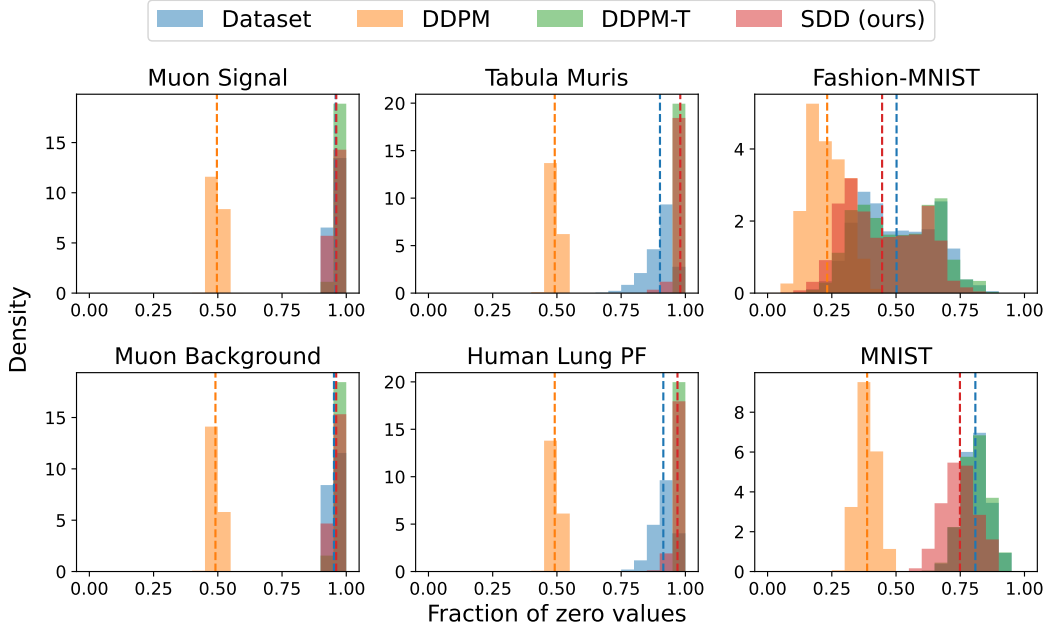


Figure 6: Shown are the sparsity density histogram (20 bins) and the average sparsity (dashed vertical line) of the dataset and generated datapoints using DDPM, DDPM-T, and SDD. The sparsity level of DDPM does not resemble the real data, while DDPM-T shows less diversity and overshoots in the upper parts of the distribution, and the proposed SDD matches it more closely.

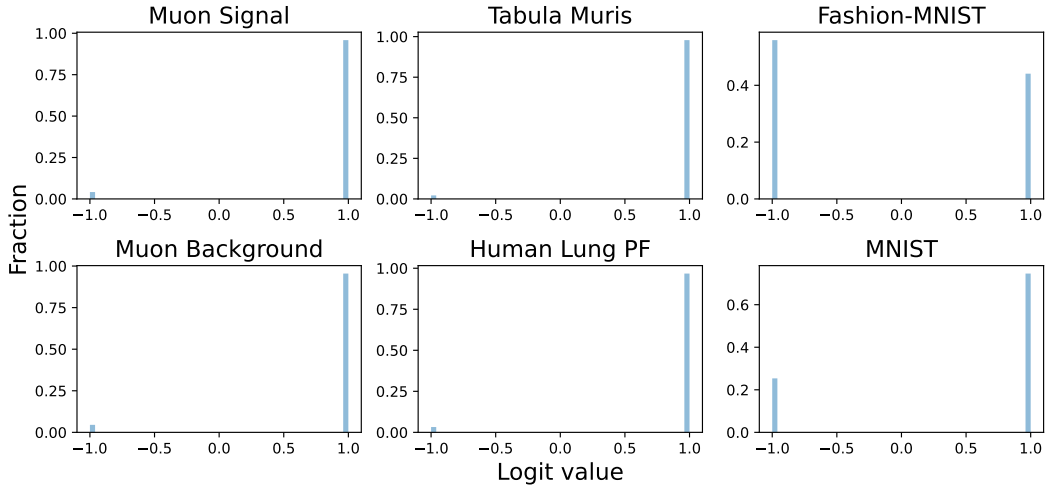


Figure 7: The histogram distribution shows 50 bins of the logits for sparsity bits for datapoints using SDD. The sparsity bits are extremely concentrated towards -1 and 1, which shows that discrete variables can be reliably diffused alongside continuous variables.

Figure 9, reinforce these findings. Both DDPM and DDPM-T yield relatively uniform activations across the image, whereas SDD-DDPM captures the expected patterns: a uniform cylindrical distribution in the signal case and energy concentrated near the muon for background events, consistent with real calorimeter data.

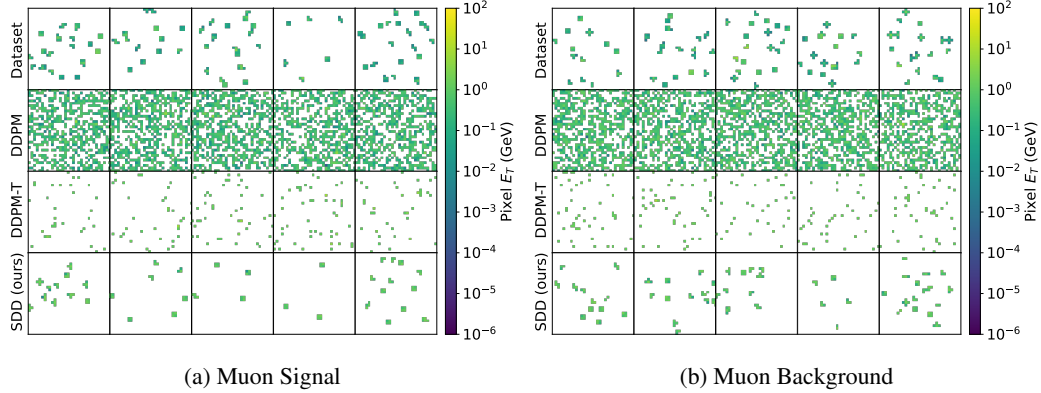


Figure 8: Generative samples for a muon isolation task from particle physics. Each panel shows calorimeter images of signal (left) and background (right) events. Rows show: (1) real data, (2) DDPM samples, (3) DDPM samples thresholded to match dataset sparsity (DDIM-T), and (4) SDD samples. Pixel intensity reflects deposited energy in GeV; white indicates zero energy. DDPM and DDPM-T fail to capture the dataset’s sparse, localized structure, while SDD closely matches the physical patterns.

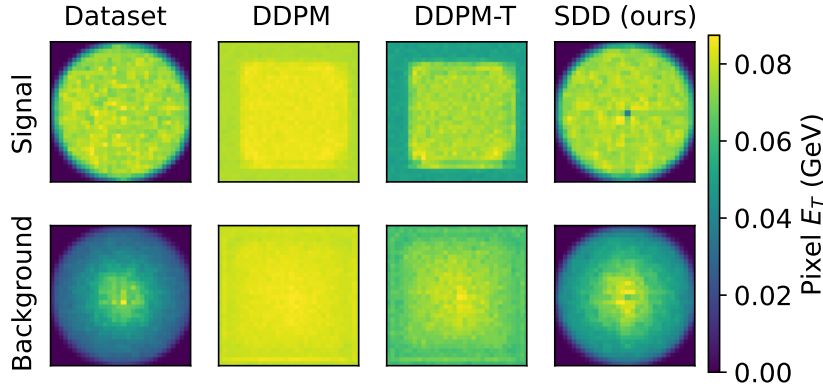


Figure 9: Shown are the average calorimeter images for Muon Signal and Muon Background. DDPM and DDPM-T fail to generate realistic data, while SDD succeeds. Linear scale to reveal the signal and background differences.

E Further results for biology: scRNA data generation

Figure 10 shows UMAP visualizations for the Tabula Muris and Human Lung Pulmonary Fibrosis datasets generated using DDPM. The trends mirror those observed with DDIM (Figure 5). Specifically, DDPM-generated samples show minimal overlap with the real cell populations, indicating limited biological realism. The thresholded variant, DDPM-T, moves the generated cluster closer to the real data manifold but at the cost of reduced diversity. In contrast, SDD-DDPM samples exhibit substantial overlap with the true cell populations, capturing both structure and diversity more faithfully. These results confirm that the benefits of sparsity-aware diffusion extend to DDPM-based models in the biological domain.

F Detailed results for sparse image generation

As discussed in Section 4.5, the visual quality of generated images for Fashion-MNIST and MNIST is largely comparable across all methods—DDIM, DDPM, their thresholded counterparts (DDIM-T and DDPM-T), and SDD. To complement these observations, Figures 11 and 12 provide detailed visualizations of the corresponding sparsity patterns. While DDIM, DDPM, and their thresholded

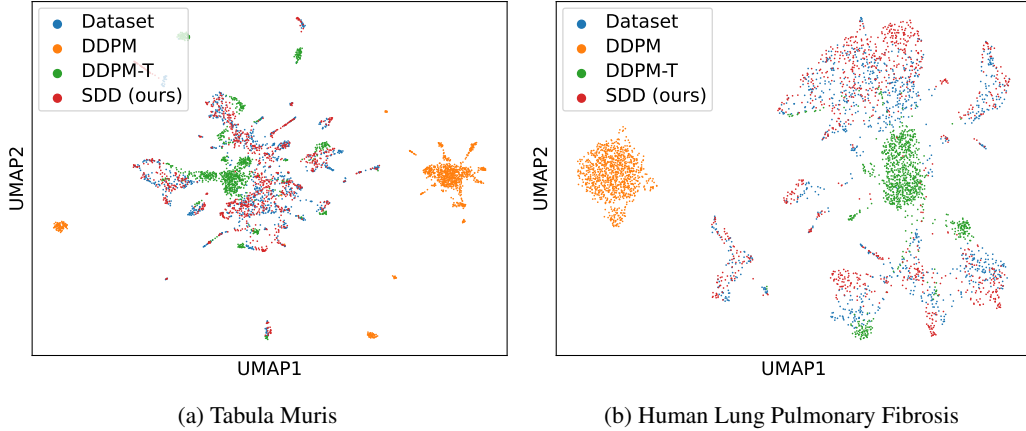


Figure 10: Shown are two dimensional UMAPs of Tabula Muris and Human Lung Pulmonary Fibrosis, and the respective DDPM, DDPM-T, and SDD generated samples. DDPM and DDPM-T show little to no overlap with the respective dataset while SDD shows significant overlap.

Table 4: Shown are the FID scores for sparse image generation. The results are similar for all considered settings.

	FASHION-MNIST	MNIST
DDPM	25.62	23.35
DDIM	24.11	23.68
DDPM-T	25.83	23.82
DDIM-T	25.72	24.04
SDD DDPM	27.81	25.37
SDD DDIM	26.37	25.69

versions produce images that appear visually plausible, closer examination reveals discrepancies in how well they capture the underlying sparsity structure of the datasets.

In particular, thresholded models such as DDIM-T and DDPM-T often fail to reproduce the fine-grained noise and soft sparsity transitions present in real data. For Fashion-MNIST, these models tend to eliminate subtle pixel activations near the edges, leading to overly clean object contours. In MNIST, the digits generated by DDIM-T and DDPM-T are noticeably narrower, lacking some of the variability found in true samples. These limitations underscore the fact that simple thresholding, while improving sparsity alignment on average, can suppress important structural variation in the data.

By contrast, SDD not only maintains competitive visual quality but also more accurately reproduces the sparsity distributions and edge-region behavior of real images. This highlights the advantage of explicitly modeling sparsity rather than relying on post-hoc thresholding to enforce it.

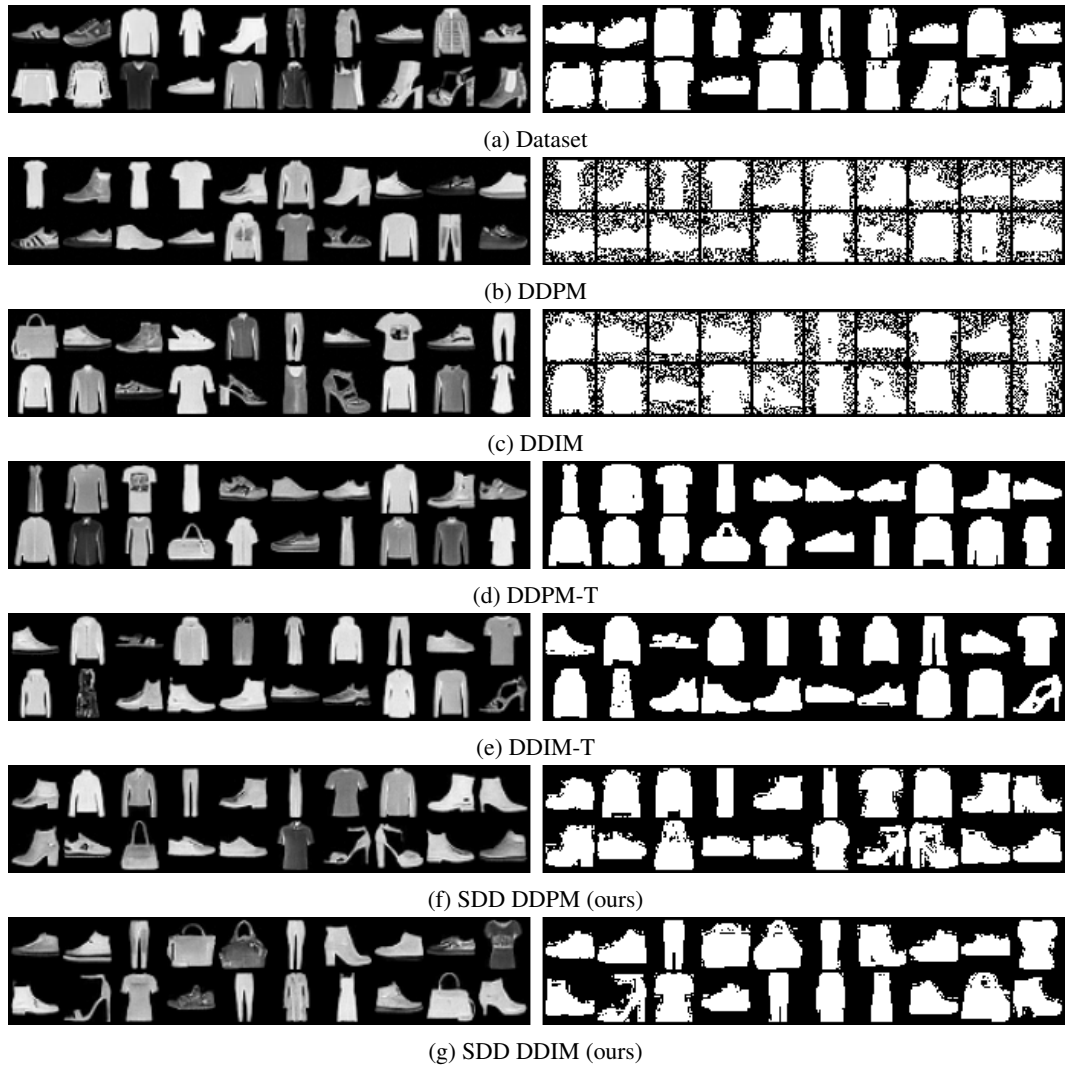


Figure 11: Shown are, from left to right, in the first row: Fashion-MNIST images sampled from the dataset, DDIM sampled images, thresholded DDIM sampled images (DDIM-T), and SDD sampled images. The second row contains the respective sparsity information. Despite highly visually similar images, DDIM fails to reflect the sparsity, whereas the proposed SDD has a similar sparsity to the images from the dataset.

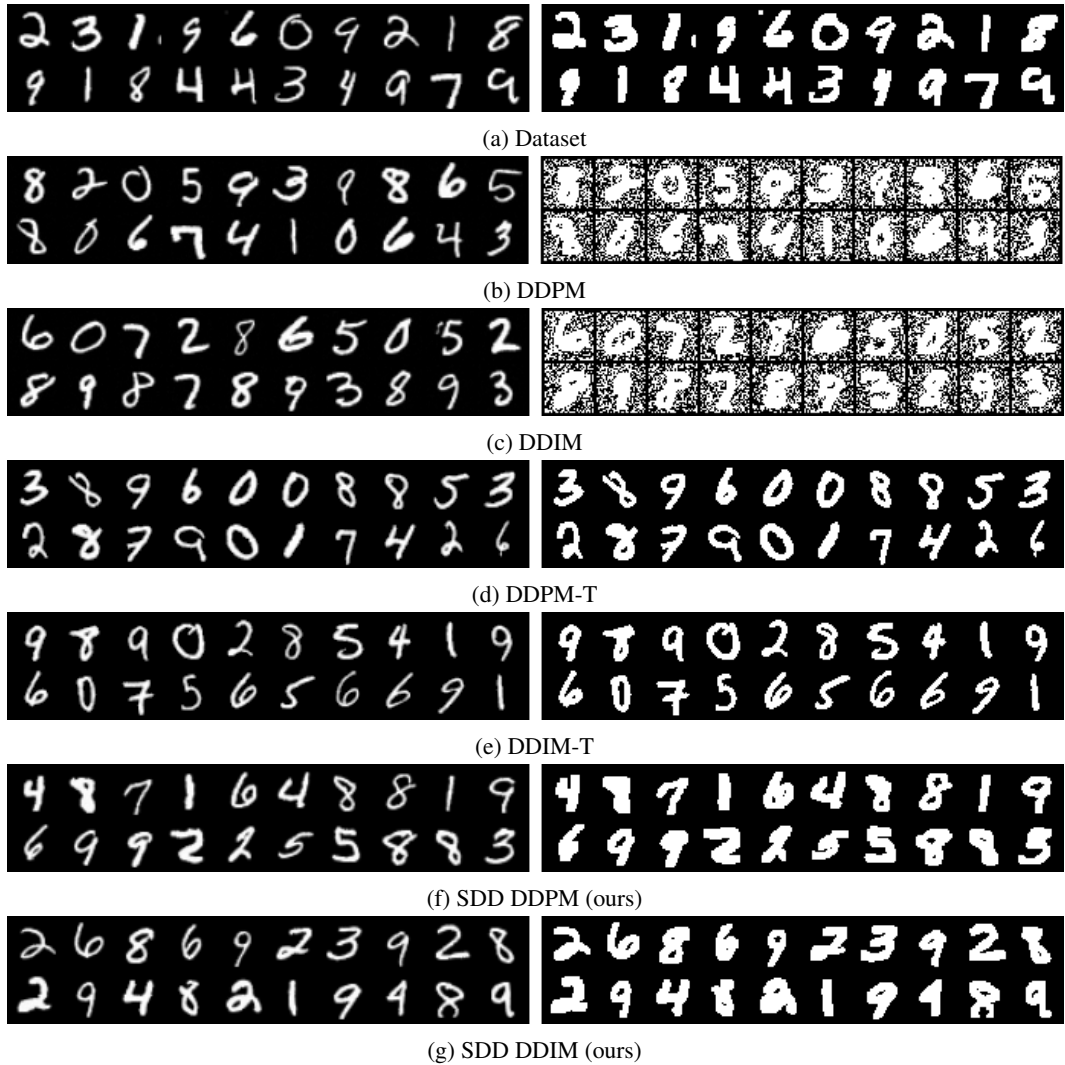


Figure 12: Shown are dataset and model sampled images on the left and the respective sparsity information. Despite highly visually similar images, DDIM and DDPM fail to reflect the sparsity, DDIM-T and DDPM-T show narrower sparsity whereas the proposed SDD DDPM and SDD DDIM have a similar sparsity as the images from the dataset.